




# Bioactive glass doped with zinc-based metal–organic frameworks (Zn/MOF) nanoparticles for antibiotic delivery applications

Manar M. Ahmed<sup>1</sup> · Areg E. Omar<sup>2</sup> · Heba S. Zayed<sup>2</sup>  · Mona Moaness<sup>3</sup>

Received: 31 December 2023 / Accepted: 1 February 2024 / Published online: 2 March 2024  
© The Author(s) 2024

## Abstract

Zn-MOF/bioactive glass nanoparticles were successfully prepared using quick–alkali-modified sol–gel and tested for gentamicin drug delivery. Samples of 0 and 0.8 mol% Zn MOF contents (BG and BG/Zn MOF, respectively) were characterized using XRD, FTIR, TEM, and SEM/EDX. In addition, zeta characteristics and surface area parameters were also evaluated. Moreover, the cell viability of the prepared samples was tested against the osteosarcoma MG-63 cell line to evaluate the ability of prepared samples for bone regeneration. In addition, the antimicrobial activity of glass samples with and without antibiotics was determined against different microorganisms. Finally, the samples were loaded with gentamicin drug, and drug release profile and kinetics were studied too. XRD and FTIR results confirmed the physicochemical properties of the prepared samples. TEM results showed that particles were in the nano-sized range in both samples; however, the presence of Zn MOF increased the dispersity of particles. Both samples were bioactive, as indicated by hydroxyapatite formation on their surfaces. Cytotoxicity estimation of prepared materials exhibited their safe and nontoxic nature. BG/Zn MOF sample demonstrated prolonged drug release and excellent antimicrobial activity in comparison to BG alone. Therefore, the present study provides promising preliminary results regarding the usage of BG/Zn MOF nanoparticles loaded with gentamicin as an effective approach for bone regeneration.

---

✉ Areg E. Omar  
aregomar8@gmail.com

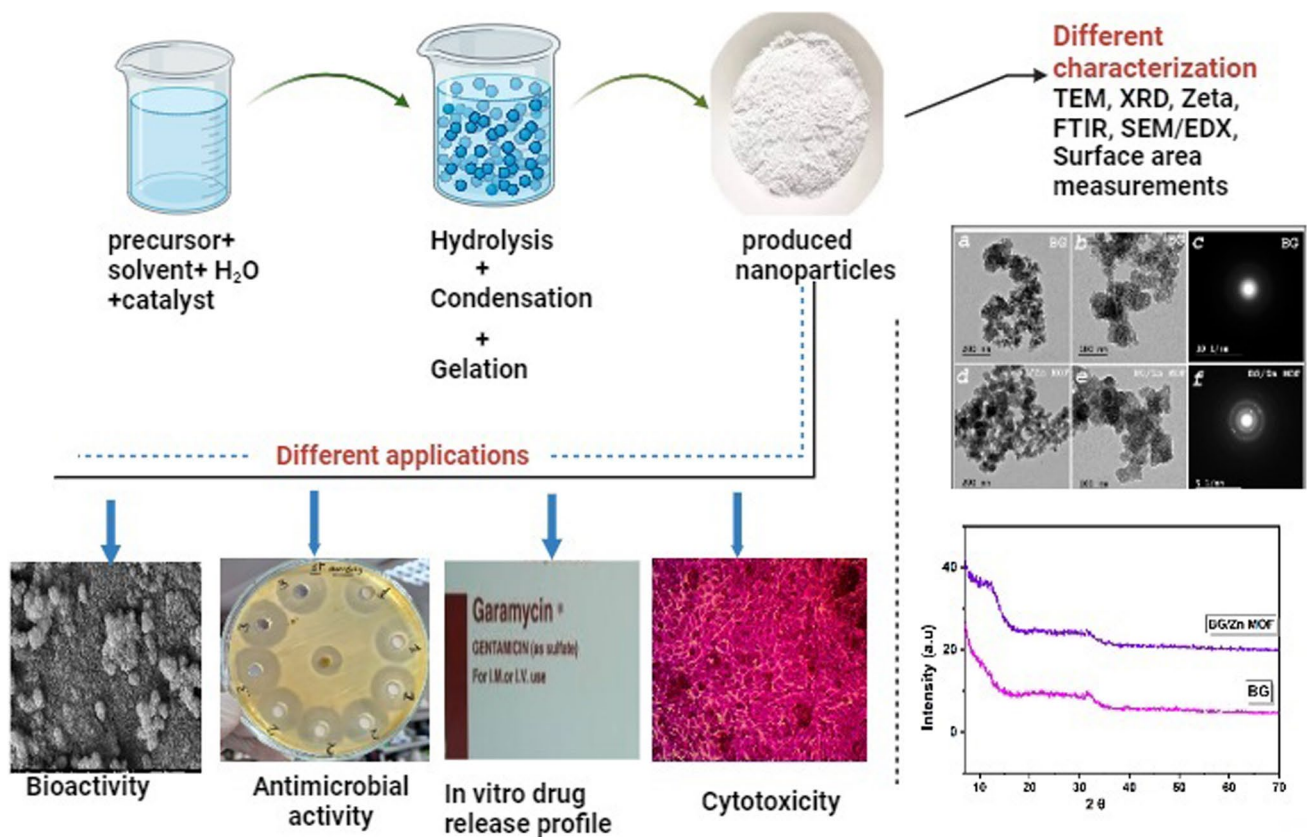
✉ Heba S. Zayed  
hebashabaan.519@azhar.edu.eg

<sup>1</sup> Glass Research Department, Advanced Materials, Technology and Mineral Resources Research Institute, National Research Centre, 33 El-Bohooth St., Dokki, Cairo 12622, Egypt

<sup>2</sup> Department of Physics, Faculty of Science, Al-Azhar University, (Girls Branch), P.O Box 11884, Cairo, Egypt

<sup>3</sup> Refractories, Ceramics and Building Materials Department, Advanced Materials, Technology and Mineral Resources Research Institute, National Research Centre, 33 El Bohouth St., Dokki, PO Box 12622, Cairo, Egypt

## Graphical Abstract



## Highlights

- Bioactive glass doped with zinc-based MOF nanoparticles was prepared and characterized.
- In vitro bioactivity, antibiotic release profile, and antimicrobial properties were evaluated.
- Cytotoxicity on osteoblast-like cells was estimated.
- The produced nanoparticles showed a long-term release of gentamicin drug.
- The prepared materials had no toxic effect on cells and could be safely used as biocompatible materials for bone regeneration.

**Keywords** Nano bioactive glass (BG) · Zn/MOF · Sol–gel · Drug delivery · Cytotoxicity

## 1 Introduction

Bone is a very dynamic tissue with an intrinsic capacity for self-regeneration [1]. Nevertheless, bone self-healing is extremely impeded in large bone defects caused by tumors, necrosis, osteoporosis, and bone infection [1, 2]. Therefore, orthopedic devices or bone grafting materials must be used in these situations. However, micro-organism adhesion to grafting materials is a main cause of implant failure. Implant

infection is a severe problem that leads to bone tissue destruction and several replacement surgeries [1–5].

Antibiotics are generally used to treat bone infections, but long-term systemic antibiotics can lead to several problems. Consequently, alternative strategies for delivering antibiotics locally or targeting antibacterial nanoparticles to the infected site should be used to combat infections [3–5].

In the literature, bioactive glasses are used in different biomedical applications, such as hard and soft tissue

regeneration as well as drug delivery systems [6–8]. Bioactive glasses have unique properties in terms of excellent bioactivity and biocompatibility, which makes them useful in the fields of scaffold construction and pharmaceuticals [9]. The properties of bioactive glasses are highly dependent on their composition and preparation methods. By adjusting the compositional elements, we can control glass bioactivity, biocompatibility, degradation rates, and biological application possibilities [10, 11]. In the same context, by tuning preparation methods, we could obtain different systems with different shapes, porosities, and several sizes ranging from micron size to nano-sized glasses. However, bioactive glasses have some drawbacks, such as low mechanical strength, fracture toughness, and brittle nature.

These restrictions decrease the use of bioactive glass as a pure material. Therefore, bioactive glass was doped by other materials to enhance its properties. Recently, metal–organic frameworks (MOFs) have committed strenuous interest in biomedical applications owing to their excellent biocompatibility and biodegradation, stability, and ability to be functionalized [12–14]. Besides, MOFs are promising drug delivery systems for their tunable porosity, larger surface area, and great biodegradability [12, 15, 16].

Zn-based MOFs could be used to control the degradation rate of bioactive glass, adjust drug delivery, and increase strength. Moreover, the presence of zinc is very important. Zinc (Zn) is an essential mineral that is a component of more than 300 enzymes and it is involved in cell proliferation, differentiation, and survival. Zinc has antibacterial and anti-inflammatory properties. It has a great role in bone metabolism; zinc can enhance DNA in osteoblasts and reduce bone resorption activity. Furthermore, Nano-ZIF-8 film increased alkaline phosphatase activity, extracellular matrix mineralization, and osteogenic gene expression, according to previous studies [12, 15, 16]. Therefore, we can predict that the addition of Zn/MOF to BG may aid in the bone regeneration process.

Herein, we will fabricate nanoscaled Zn-MOF/bioactive glass composite for drug delivery applications, and investigate their physicochemical properties, in vitro apatite forming ability, cell biocompatibility, and antimicrobial effect.

## 2 Experimental method

### 2.1 Materials

Tetraethyl orthosilicate (TEOS), calcium nitrate tetrahydrate (Ca (NO)<sub>3</sub>·4H<sub>2</sub>O), and triethyl phosphate (TEP) all ≥ 98% and purchased from Fluka (Buchs, Switzerland). Ammonia solution, 33%, and nitric acid, 68%, were purchased from Merck, USA. Both nitric acid and ammonia solutions were diluted to 2 M using distilled water.

### 2.2 ZIF-8 fabrication

ZIF-8 nanoparticles (Zinc MOF, zinc methylimidazolate, 2-methylimidazole zinc salt) were previously prepared and fully characterized as described in Moaness et al. [17].

### 2.3 Preparation of nano bioactive glass (BG) and BG/Zn MOF

Nano bioactive glasses and BG/Zn MOF in the 60 SiO<sub>2</sub>–10 P<sub>2</sub>O<sub>5</sub>–(30–*x*) CaO–(*x*) ZIF-8 nanoparticles (*x*=0 and 0.8% mol%) system, with codes and compositions illustrated in Table 1, were fabricated through quick alkali-modified sol–gel technique [18]. First, TEOS, distilled water, and 2 M nitric acid (as a hydrolysis catalyst) were consecutively mixed in ethanol and the mixture was allowed to react for 60 min under continuous magnetic stirring for the acid hydrolysis of TEOS. Then, the suitable amounts of a series of reagents were added in the following sequence: TEP, Ca(NO<sub>3</sub>)<sub>2</sub>·4H<sub>2</sub>O, and ZIF-8 nanoparticles, allowing 30 min for each reagent to react completely.

The molar ratio of water/TEOS is fixed at 12/1, the ratio of H<sub>2</sub>O/Ethanol is 1/1, and the volume ratio of water/nitric acid is fixed at 6/1 [19]. To prevent particle aggregation, the mixture was then transferred into a standard ultrasonic bath operating at a frequency of 50–60 kHz, 100–200 W, and then, 2 M ammonia solution (a gelation catalyst) was dropped into the mixture under constant stirring. The gelation of the mixture took place in a few minutes. Finally, the prepared gels were dried at 60 °C for 2 days in a drying oven. The dry gel powders were calcined at 700 °C for 3 h. The calcination's heating rate was set at 3 °C/min.

## 3 Characterization of prepared samples

The morphology and size of the prepared BG as well as BG/Zn MOF were examined using high-resolution transmission electron microscopy (HR-TEM) (JEM-2100, Jeol, Japan). To form a diluted suspension, we ultrasonically dispersed the powder samples in 10 ml of distilled water, and then, small drops of this suspension were dropped on the surface of copper grids that were allowed to air dry on the surface of a

**Table 1** Codes and composition of the prepared samples

Sample code	Composition (mol %)			
	SiO <sub>2</sub>	CaO	P <sub>2</sub> O <sub>5</sub>	ZIF-8 nanoparticles
BG	60	30	10	0
BG/Zn MOF	60	29.2	10	0.8

filter paper. The grids were placed in the grid box and examined by the TEM machine. The samples were also imaged using scanning electron microscopy. In addition, elemental analyses were conducted on the above-selected samples using energy dispersive X-rays (EDX) analysis.

The characterization of the physicochemical nature of the prepared samples was performed using X-ray diffraction analysis (XRD) the XRD was carried out at a  $2\theta$  (Bragg angle) of  $5\text{--}80^\circ$ , using a Bruker D8 Advance X-ray diffractometer (Germany). The diffraction patterns were recorded at a voltage of 40 kV with a current of 40 mA, using copper ( $K\alpha$ ) radiation ( $1.5406 \text{ \AA}$ ).

The functional groups of the two synthesized samples BG and BG/Zn MOF were evaluated using Fourier transform infrared spectroscopy (FTIR). The functional groups were determined in  $400\text{--}4000 \text{ cm}^{-1}$  wavenumber range at room temperature ( $25^\circ\text{C}$ ) at a resolution of  $4 \text{ cm}^{-1}$  employing Fourier transform infrared spectrophotometer (model FT/IR-6100 type A).

The evaluation of surface charges of the synthesized samples was assessed using Zetasizer (Nano ZS, Malvern Instruments Ltd, UK). The prepared BG and BG/Zn MOF were individually suspended in distilled water, sonicated for 30–60 min, and forced to pass through a micro-filter ( $0.22 \mu\text{m}$ ). Filtered sample suspension was transferred to a measuring cell (DTS1060, Malvern). For data analysis, specific software (Version 4.0) was utilized. An electric field was applied.

In addition, surface area parameters were developed using nitrogen adsorption–desorption isotherms of an automatic analyzer (Quantachrome Nova 8, Automated Gas Sorption System, and Version 1.12).

## 4 Assessment of bioactivity

In vitro bioactivity evaluation was determined by immersing the prepared samples (BG and BG/Zn MOF) in a simulated body fluid (SBF), a water solution of various inorganic ions in a concentration close to that in human blood plasma, for estimating the formation of hydroxyapatite on the surface of the immersed samples. After 4 weeks of immersion in SBF, the discs were removed and characterized by SEM coupled with EDX, and Fourier transform infrared spectra (FTIR).

Different discs of BG and BG/Zn MOF samples were immersed into SBF and incubated at  $37^\circ\text{C}$ , pH 7.4 for different periods (1, 3, 7, 14, and 28 days). At the predetermined periods, the ionic components liberated from samples into SBF were measured either by a spectrophotometer or ICP (inductively coupled plasma). Moreover, pH changes were also examined at the same periods.

## 5 In vitro assessment of drug loading and release

Gentamicin sulfate was used as a drug model. It is a broad-spectrum antibiotic for gram-negative and gram-positive bacteria [20]. The drug was loaded into BG and BG/Zn MOF nanoparticles by immersing 0.05 g glass powder in 10 ml of gentamicin solution (0.4 mg/ml) for 24 h under stirring. Subsequently, the glass powder was collected using filter paper and dried at  $60^\circ\text{C}$ . The amounts of loaded drug were calculated using UV/Vis spectroscopy (UNICO UV2000) at wavelength 232 nm.

The drug release was determined at  $37^\circ\text{C}$  up to 28 days. The drug release profile was calculated by soaking drug-loaded samples in 10 ml of phosphate-buffered solution (PBS, pH 7.4). 2 ml of PBS was collected at the predominant time (1, 3, 6, 12 h, 1, 2, 4, 7, 10, 14, 28 d), then replaced with 2 ml of fresh phosphate buffered solution. These samples were kept at  $20^\circ\text{C}$  for further investigation. The amount of released drug from samples as well as the calibration curve was estimated using a UV spectrophotometer at a wavelength of 232 nm.

## 6 Cytotoxicity assessment

Human osteosarcoma (MG63) cells were used to evaluate the cytotoxicity of the samples. MG63 cells were obtained from Nawah Scientific Inc., (Mokatam, Cairo, Egypt).

Cell viability was assessed with the aid of SRB assay. Cell viability becomes assessed via SRB assay. Aliquots of  $100 \mu\text{l}$  cell suspension ( $5 \times 10^3$  cells) have been plated in 96-well plates and incubated in whole medium for 24 h. Cells were treated with some other aliquot of  $100 \mu\text{L}$  media containing numerous concentrations of the drug. After drug exposure, cells were fixed by way of changing media with  $150 \mu\text{l}$  of 10% TCA and incubated at  $4^\circ\text{C}$  for 1 h. The TCA solution turned into eliminated, and the cells were washed 5 times with distilled water. Aliquots of  $70 \mu\text{l}$  SRB solution (0.4% w/v) have been added and incubated in a dark area at room temperature for 10 min. Plates were washed 3 times with 1% acetic acid and allowed to air-dry overnight. Then,  $150 \mu\text{l}$  of TRIS (10 mM) was added to solubilize the protein-bound SRB stain; the absorbance was measured at 540 nm using a limitless F50 microplate reader (TECAN, Switzerland). The study protocol was approved and examined according to the ethical guidelines of the medical research Ethics Committee of the National Research Centre, Dokki-Egypt. Approval number: 34110723.

## 7 Assessment of antimicrobial efficacy of BG and Zn MOF/BG

Antimicrobial activities of BG, Zn MOF/BG, drug @BG, drug @ BG/Zn MOF, and drug alone were tested qualitatively against a variety of human pathogens. The tested microbial cultures were gram-positive bacteria (*Staphylococcus aureus* ATCC 6538), gram-negative bacteria (*Escherichia coli* ATCC 25922), and pathogenic yeast (*Candida albicans* ATCC 10231). These microbial species were delivered by the American Type Culture Collection (ATCC, Rockville MD, USA) and Northern Utilization Research and Development Division, United State Department of Agriculture, Peoria, Illinois, USA (NRRL). The microbial cultures were prepared from fresh overnight broth cultures using a nutrient broth medium that was incubated at 37 °C.

The inoculum volume of this pathogenic strain was prepared and adjusted to approximately 0.5 McFarland standard ( $1.5 \times 10^8$  CFU/ml) [21], and a 25.0 µl inoculum volume of each microorganism strain was inoculated separately into each plate containing 20.0 ml of sterile nutrient agar (NA) medium. In addition, 25.0 µl of each of the bacterial and fungal suspensions were inoculated separately into each 100.0 ml conical flask containing 25.0 ml of sterile nutrient broth (NB) medium. The samples were applied After the media cooled and solidified on a 0.9 cm well of that inoculated agar plates which were organized formerly utilizing 1.0 cm cork borer applying the Well Diffusion Method, in this technique each well was filled with 100.0 µl of every sample one after the other [22]. These inoculated plates were located within the refrigerator for 1 h for extra diffusion of those samples, followed by incubation at 37 °C for 24 h, and then antimicrobial activity was estimated three times as inhibition zone diameter in millimeters.

### 7.1 Statistical analysis

Three samples were used for each of the quantitative experiments with each measurement finished in duplicate to verify the reproducibility. Every parameter was expressed as the mean of all values and their standard deviations. Statistical analysis is completed using one way ANOVA test. Values of  $p < 0.05$  had been taken into consideration as significant (\*) and  $p < 0.0001$  had been considered very significant (\*\*).

## 8 Results and discussion

### 8.1 Particle size analysis via transmission electron microscopy (TEM)

The morphology and particle size of BG and BG/Zn MOF were determined via HR-TEM, as indicated in Fig. 1. In

both samples, all particle sizes were in the nano-scale range (below 100 nm).

Figure 1a, b illustrates that the BG sample contains nanoparticles in the size range from 8 to 35 nm. The incorporation of Zn/MOF into BG has increased the size of particles to become in the range of 20–90 nm. Moreover, it increases the dispersity of particles, as shown in Fig. 1d, e.

Micrographs showed the amorphous nature of BG, as exhibited in Fig. 1c, and the crystallinity of BG/Zn MOF (Fig. 1f), as demonstrated by lattice planes with d-spacing values from 2 to 6 nm.

### 8.2 Structural analysis

The XRD patterns of prepared samples are presented in Fig. 2a. There was no crystal phase and both samples have an amorphous structure. There was a diffuse halo between 12 and 22° (2θ), this halo refers to amorphous silica [23]. Another weak peak observed at  $2\theta = 31.7^\circ$  can be attributed to the formation of the orthophosphate regions during synthesis, as reported in previous studies with the same composition [24]. These findings suggest that even after Zn/MOF was incorporated into BG, the predominantly amorphous structure was maintained. meanwhile, there is a weak peak in BG/Zn Mof appeared at  $2\theta = 11.7^\circ$  related to Zn/MOF as reported in [25, 26].

FTIR spectra are shown in Fig. 2b. The results indicate that all samples have comparable FTIR spectra, and the incorporation of Zn/MOF into BG does not alter the structure of samples. FTIR spectra have wavenumbers at 460, 558, 600, 797, 950, and 1064  $\text{cm}^{-1}$ . Si–O bending can be seen at wavenumber 460  $\text{cm}^{-1}$ . The band at 1064  $\text{cm}^{-1}$  refers to P–O antisymmetric stretching which could have overlapped with that of Si–O–Si asymmetric stretching, while symmetric stretching of Si–O is observed at wavenumber 797  $\text{cm}^{-1}$ . The shoulder around 950  $\text{cm}^{-1}$  could be related to Si–O bonds containing non-bridging oxygen (Si–O–NBO) [18, 19, 27]. Finally, 558 and 600  $\text{cm}^{-1}$  are due to orthophosphate groups [24].

### 8.3 Zetasizer characterizations

To evaluate the stability of particle suspensions, surface charge measurements were determined for all the prepared samples loaded with gentamicin and drug-free NPs.

Zeta potential values were negative for all examined samples, as illustrated in Fig. 3. Negative charge zeta potential is an essential issue for cell adhesion, protein adsorption, and good drug delivery as described previously [28–32]. Moreover, zeta potential values indicated that all nanoparticles have good colloidal stability either with or without the drug. In the literature, zeta potential is considered stable if it has values above +30 mV or less than –30 mV [33].

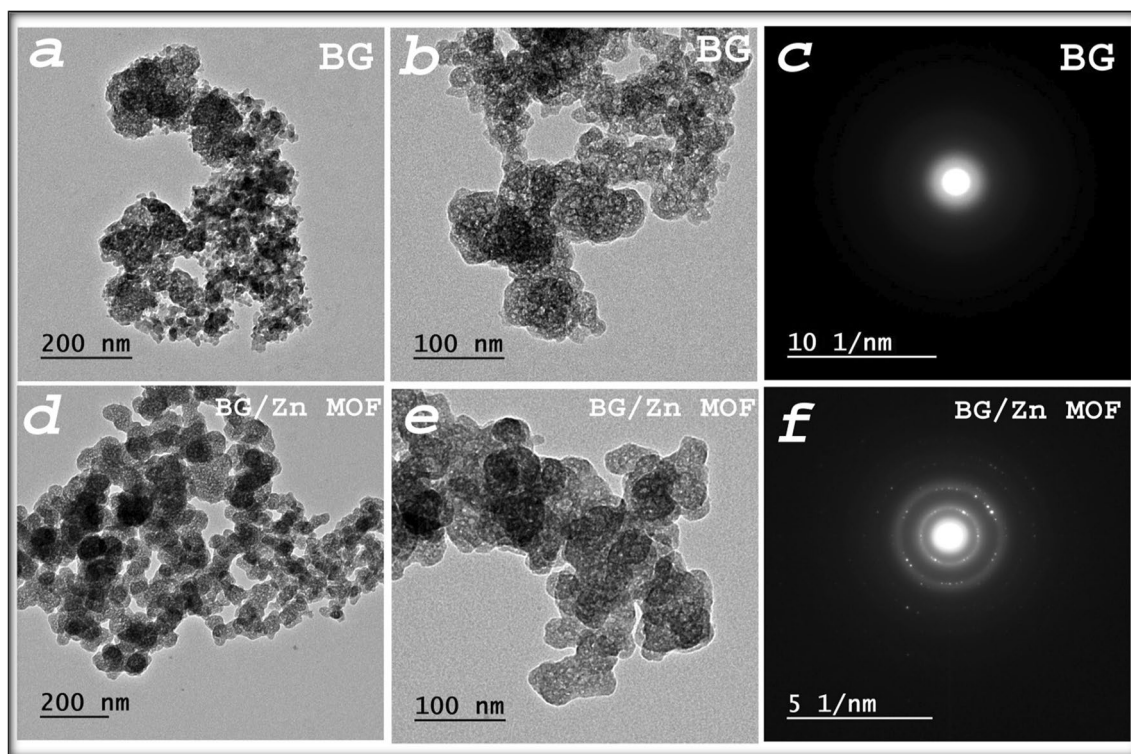


Fig. 1 TEM micrographs and diffraction pattern recorded for BG (a–c) and BG/Zn MOF (d–f)

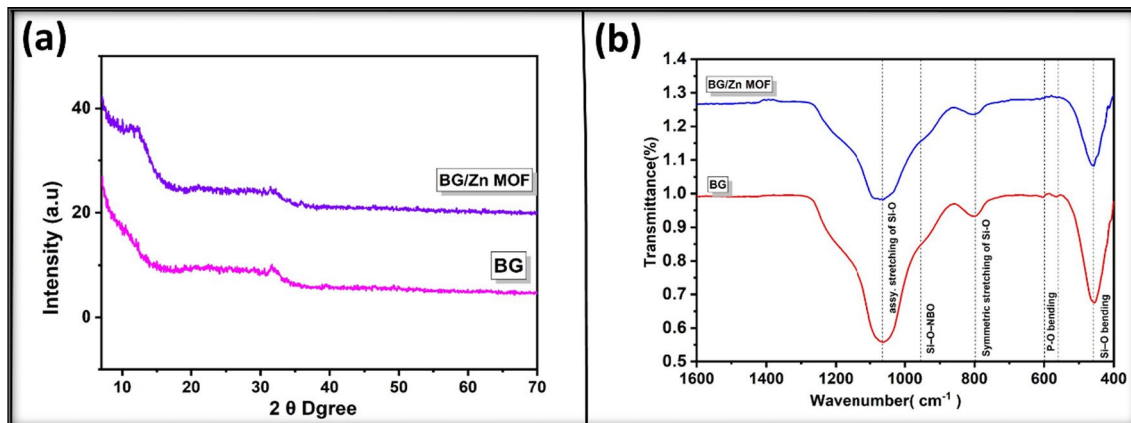


Fig. 2 a XRD analysis b FTIR of the prepared samples BG and BG/Zn MOF

In drug-free nanoparticles, the zeta potential values were  $-15.2$  and  $-15.3$  mV for BG and BG/Zn MOF, respectively. After drug-loaded nanoparticles, the zeta potential values were  $-2.86$ ,  $-15.9$ , and  $-15.5$  mV for gentamicin, BG loaded with drug, and BG/Zn MOF loaded with drug, respectively.

#### 8.4 Surface area parameters evaluations

Specific surface area measurements are critical parameters for drug delivery systems, because they dictate various aspects such as pore size and volume, which govern

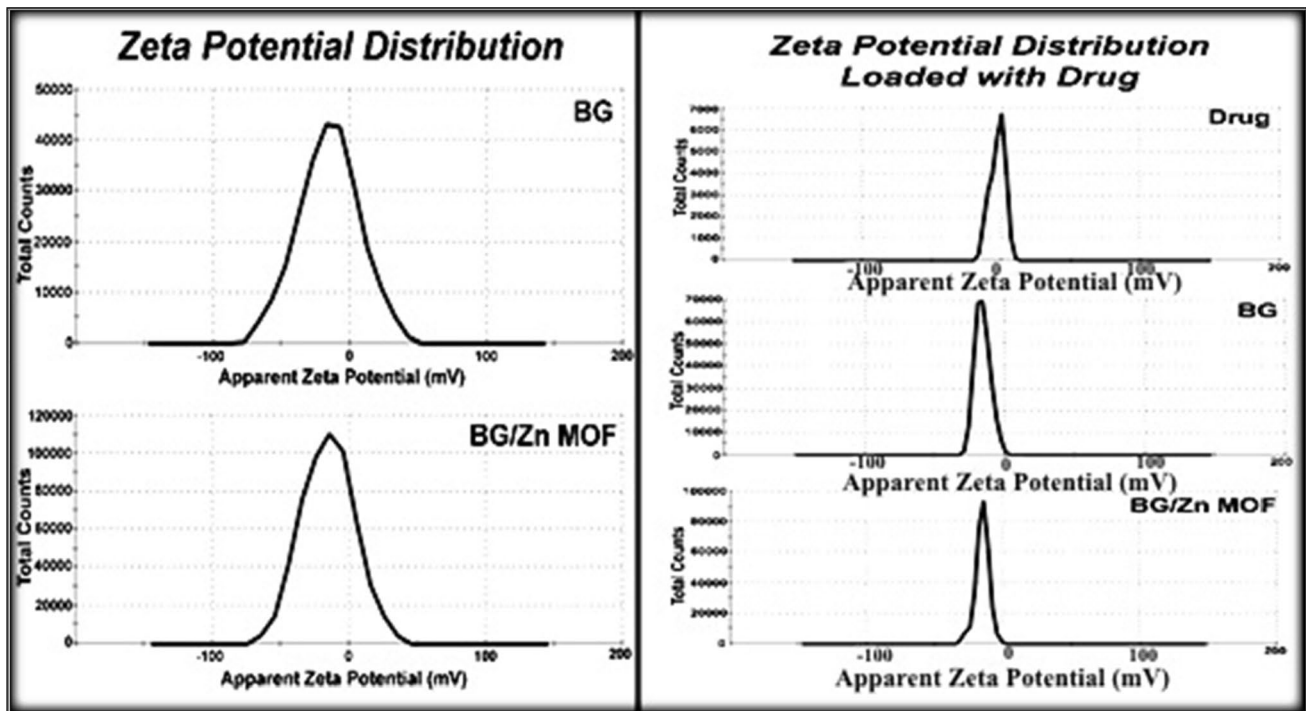


Fig. 3 Zeta potential distribution for prepared samples with and without drug

the characteristics and behavior of drug loading and release from porous nanomaterials [34, 35].

Figure 4 illustrates the nitrogen adsorption–desorption isotherms and pore size distribution of BG and BG/Zn MOF samples. As shown in Fig. 4a, c, both samples had mesoporous structures of the type IV isotherm, according to IUPAC classification. In addition, the pore width is in the range of 2–40 nm (see Fig. 4b, d), the pores are characterized by H3-type hysteresis loop, for nanomaterials (non-regular, slit-shaped, and interconnective pores) [36].

Specific surface area, pore diameter, and total pore volume of prepared samples are illustrated in Table 2. Specific surface area values had increased to 138.451 (m<sup>2</sup>/g) by adding zinc MOF nanoparticles to BG in comparison to BG alone (128.651 m<sup>2</sup>/g), as presented in Table 2.

This large surface area is very important for tissue regeneration, cell proliferation, and migration [37]. Moreover, it is a vital parameter for drug loading and release from porous nanomaterials [34, 35].

The average pore diameter reported for nanoparticles was 4.08, and 3.8617 nm for BG and BG/Zn MOF, respectively. It was observed that the pore size was slightly increased after adding zinc MOF to bio-glass. On the other hand, the total pore volume reported for BG and BG/Zn MOF nanoparticles was 0.618484 and 0.527947 (cm<sup>3</sup>/g), respectively, which approves higher pore volumes for both samples especially those containing zinc MOF. In general, the total pore

volume decreases as surface area increases as described in other papers [17, 38].

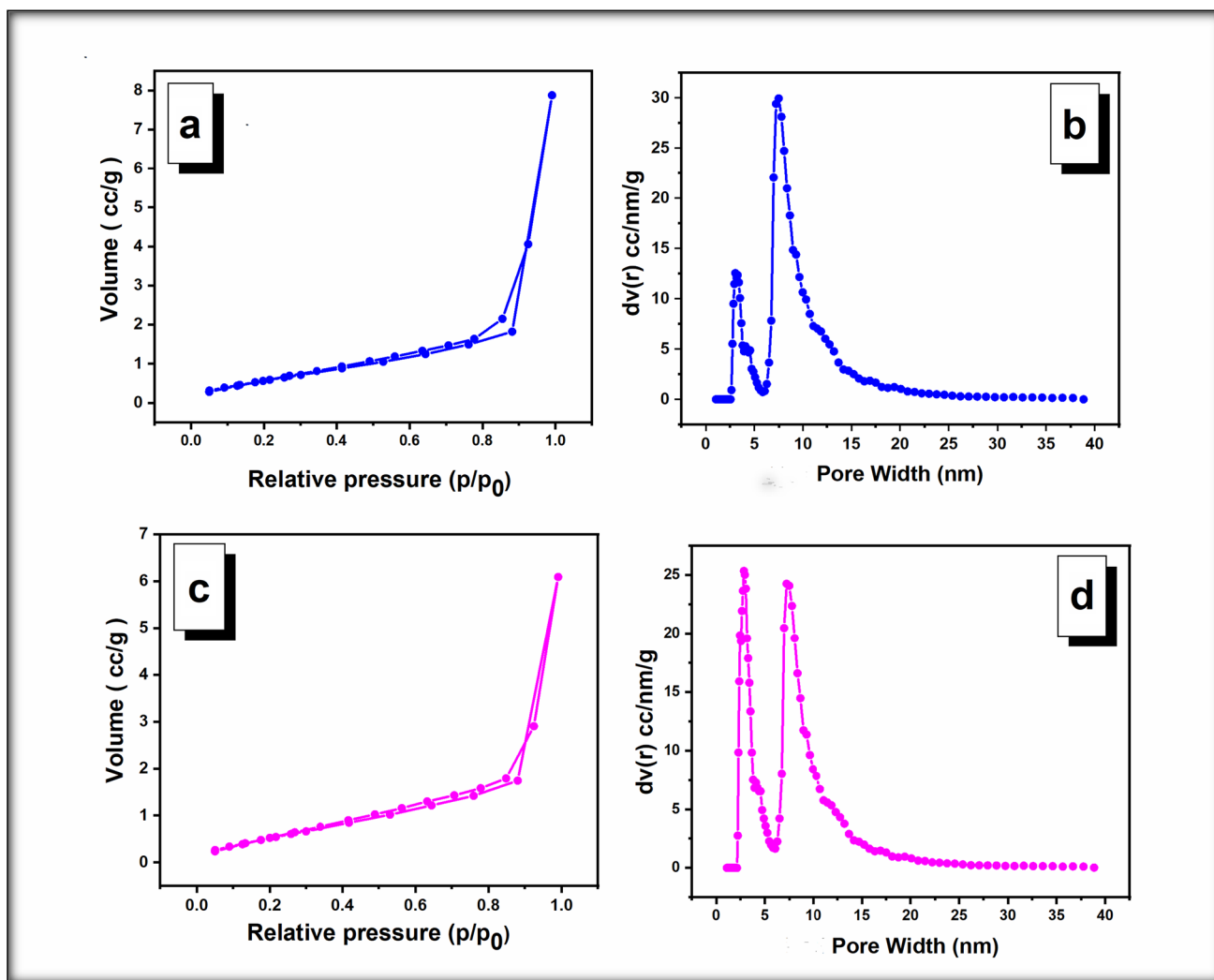
## 8.5 Scanning electron microscope with EDX before SBF immersion

Figure 5 represents the SEM micrographs and corresponding EDX spectra of BG and BG/Zn MOF Samples before SBF soaking. The surface in the BG sample showed a heterogeneous surface with random particles. However, the sample containing Zn MOF revealed a more homogenous surface, as illustrated in Fig. 5. The EDX spectrum shows the presence of Si, P, and Ca as the main elements of glass composition, while in BG/Zn MOF sample, the main elements are Si, P, and Ca in addition to Zn.

## 8.6 In vitro bioactivity evaluation

### 8.6.1 SEM/EDX after SBF soaking

SEM micrographs of the surface of prepared samples BG and BG/Zn MOF in addition to EDX analysis, after immersion for 4 weeks in SBF, are shown in Fig. 6. As illustrated from micrographs, spherical particles fully covered the surface of both samples. The EDX analysis for these figures illustrated that these layers may be stoichiometric apatite with a Ca/P



**Fig. 4** Isotherm and pore size distribution of **a, b** BG and **c, d** BG/Zn MOF nanoparticles

**Table 2** Pore diameter, specific surface area, and total pore volume for prepared nanoparticles

Sample	Pore diameter (nm)	Specific surface area (m <sup>2</sup> /g)	Total pore volume (cm <sup>3</sup> /g)
BG	3.8349	128.651	0.618484
BG/Zn MOF	3.8617	138.451	0.527947

ratio of 1.85, and 1.76 for BG and BG/Zn MOF, respectively. The presence of Zn MOF improved hydroxyapatite formation and caused Ca/P to approach stoichiometric apatite value (Ca/P=1.67). Ion dissolution from glass samples initiates the formation of hydroxyapatite layer [39].

### 8.6.2 FTIR analysis after SBF immersion

FTIR spectra of the prepared samples after 4 weeks of SBF soaking are exhibited in Fig. 7. Both samples illustrate the creation of an apatite layer as showed by the presence of characteristic bands of hydroxyapatite [40–42].

After SBF treatment, there are new peaks developed for carbonate modes (C–O  $\nu_3$ ), and (C–O  $\nu_2$ ) that appeared at 1413 and 870  $\text{cm}^{-1}$ , respectively. In addition, the clarity and intensity of the phosphorus-characteristic bands increased. (P–O Bend-Crystalline), (P–O Bend-Amorphous), [P–O ( $\nu_1$ )] and [P–O ( $\nu_3$ )], appeared at wavenumbers 560, 602, 960, 1025  $\text{cm}^{-1}$ , respectively. These results confirmed the formation of crystalline hydroxyapatite on BG and BG/Zn MOF disks.



**Fig. 5** SEM micrographs and corresponding EDX spectra of BG and BG/Zn MOF Samples before SBF soaking

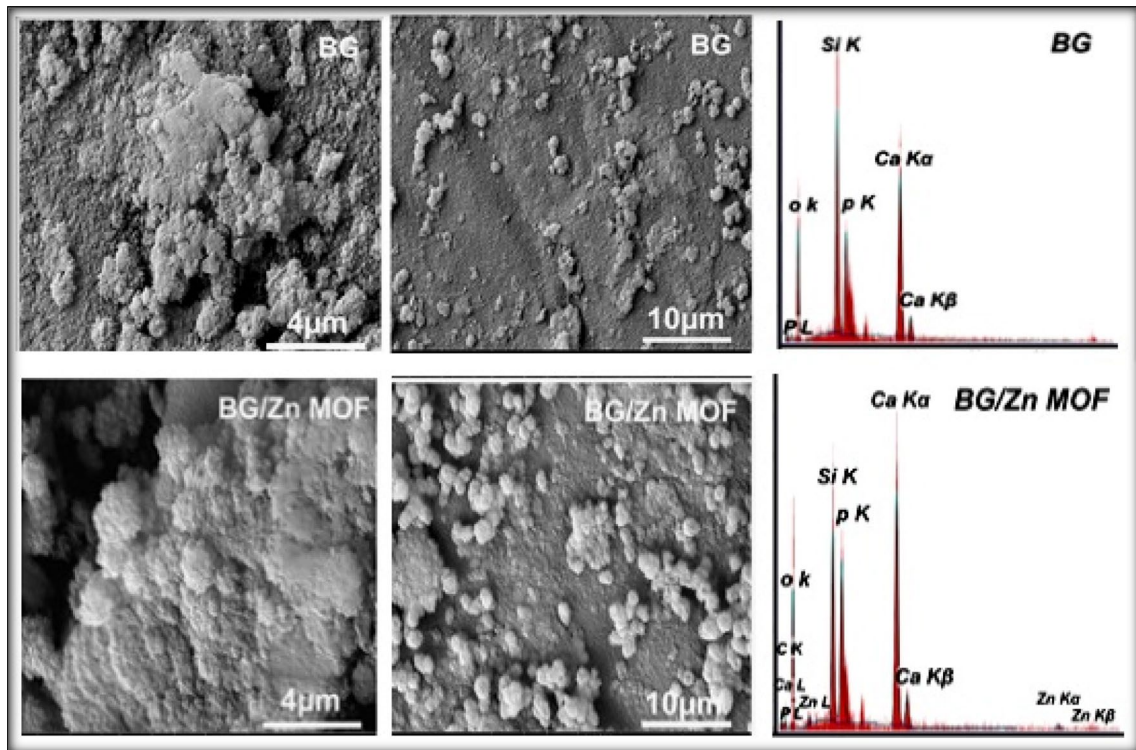
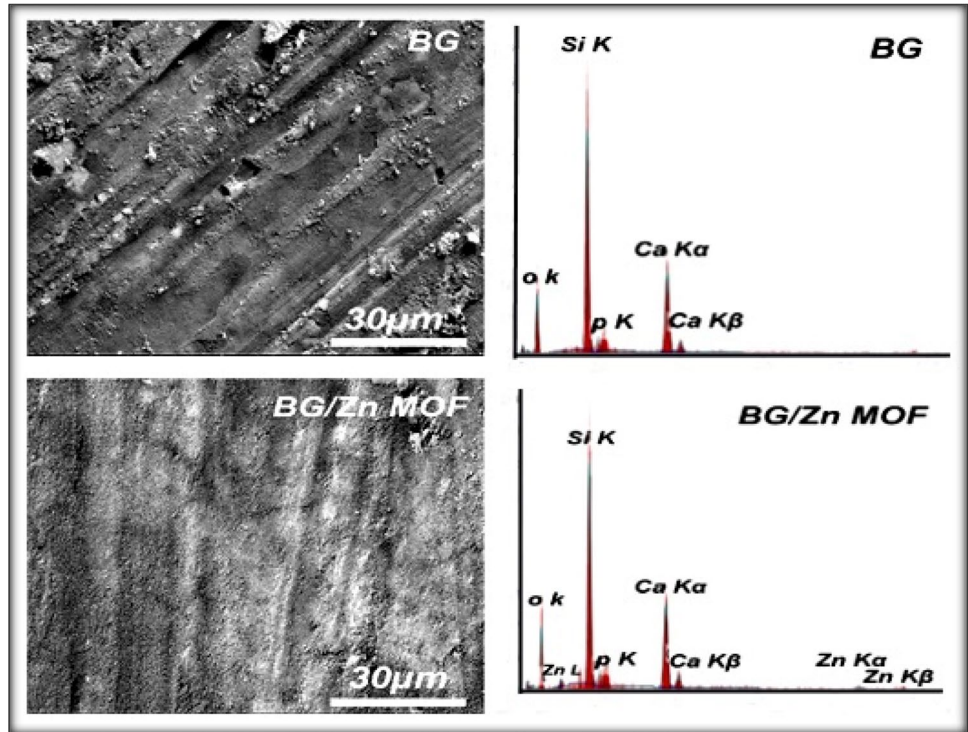


**Fig. 6** SEM photos and corresponding EDX spectra of BG and BG/Zn MOF samples after SBF immersion

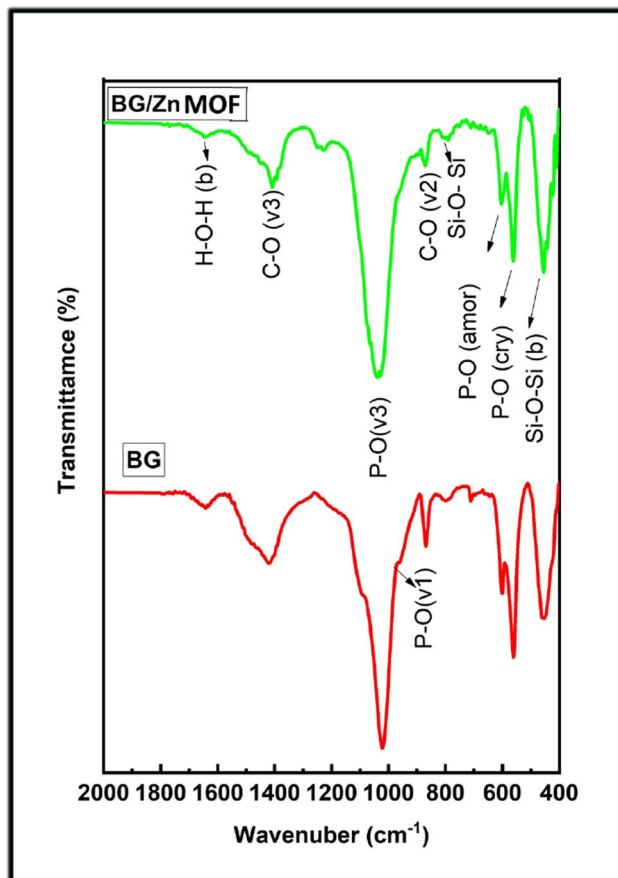


**Fig. 7** FTIR spectra of the prepared samples after 4 weeks of SBF immersion

## 8.7 Ion release and pH change analysis

The variation of concentrations of calcium, phosphorus, silica, and zinc ions, released from samples in SBF solution, as well as pH changes, is measured at different periods. Changes in SBF ion concentrations are examined as a sign of hydroxyapatite formation on sample surfaces.

Figure 8 shows the dissolution profiles of prepared BG and BG/Zn MOF samples in SBF at different periods. It is related to the concentrations of the elements Ca, P, Si, and Zn as well as the change in pH values. As shown in Fig. 8a, there is a rise in calcium ion concentration during the first three days reaching the highest values of 27.4 and 24.5 ppm for BG and BG/Zn MOF, respectively. After 4 weeks of immersion, the calcium ion concentration decreased to 11.8 and 13.6 ppm for BG and BG/Zn MOF, respectively.

The increase in ion concentration in the first three days may be due to the exchange of calcium ions with  $H^+$  or  $H_3O^+$  ions in the solution. The subsequent decrease in calcium ion concentration may be due to the deposition of  $Ca^{+2}$  ions on

the surface of the as-prepared materials due to the negative charge attraction of Si–OH groups [43].

Figure 8b displays the change in phosphorus ion in SBF at different periods of sample soaking. For both prepared samples there is a significant decrease in P ion, reaching a minimum value of 1.16, and 0.84 ppm, for BG and BG/Zn MOF, respectively, after 7 days of soaking. After 4 weeks of immersion, the phosphorus ion, concentrations in both samples became close to each other (1.90 and 1.82 ppm for BG and BG/Zn MOF, respectively).

The appearance of Ca and P ions in the SBF solution is correlated with two opposed processes: the release of Ca and P from the glass network results in the increase of their concentration in the SBF; the consumption of Ca and P during the formation of apatite layer causes the decrease of their concentration. Thus, the change in Ca concentration indicates that the release of Ca ions is higher than their consumption in the early stage of soaking. The decrease in phosphorus ions, especially during the first soaking periods, indicates that the consumption of phosphorus in the formation of hydroxyapatite is higher than its release from the samples [44].

SBF primer fluid does not contain silicone. Silicon ions can appear in SBF due to the loss of soluble  $Si(OH)_4$  by breaking Si–O–Si bonds under glass lattice interactions with SBF liquid.

For the BG and BG/Zn MOF samples, as shown in Fig. 8c, the concentration of silicon released in the solution increased rapidly and reached the highest value (13.2 ppm) for the BG sample after 7 days, while for the BG/Zn MOF sample, it reached the highest value (13.8) after 10 days of soaking in SBF. For both samples at the end of the soaking time, the silicon ion concentration is very close (11 and 10.8 ppm for BG and BG/Zn MOF, respectively).

The release of silicon ions signals the first stage of dissolution by breaking up the outer silica layers of the network. Solid silica dissolves in the form of monosilicic acid  $Si(OH)_4$  in the solution resulting from the breaking of Si–O–Si bonds and the formation of Si–OH (silanols) at the glass–solution interface [44, 45].

For the sample BG/Zn MOF that contains Zn, the release of Zn ion in SBF is evaluated, as observed in Fig. 8d. It is clear from the figure that the soaking of BG/Zn MOF sample leads to the appearance of Zn ion in the SBF. The Zn ion concentration in SBF increased by time of soaking and reached to maximum value after 7 days of incubation (0.043 ppm). During the remaining period of incubation, the release of Zn ions decreased and reached to value of 0.018 ppm after 28 days. This decrease in Zn ion during the latest period of soaking may be due to the precipitation of hydroxyapatite on the sample surface. Although the low Zn content in BG/Zn MOF sample is favorable from the view

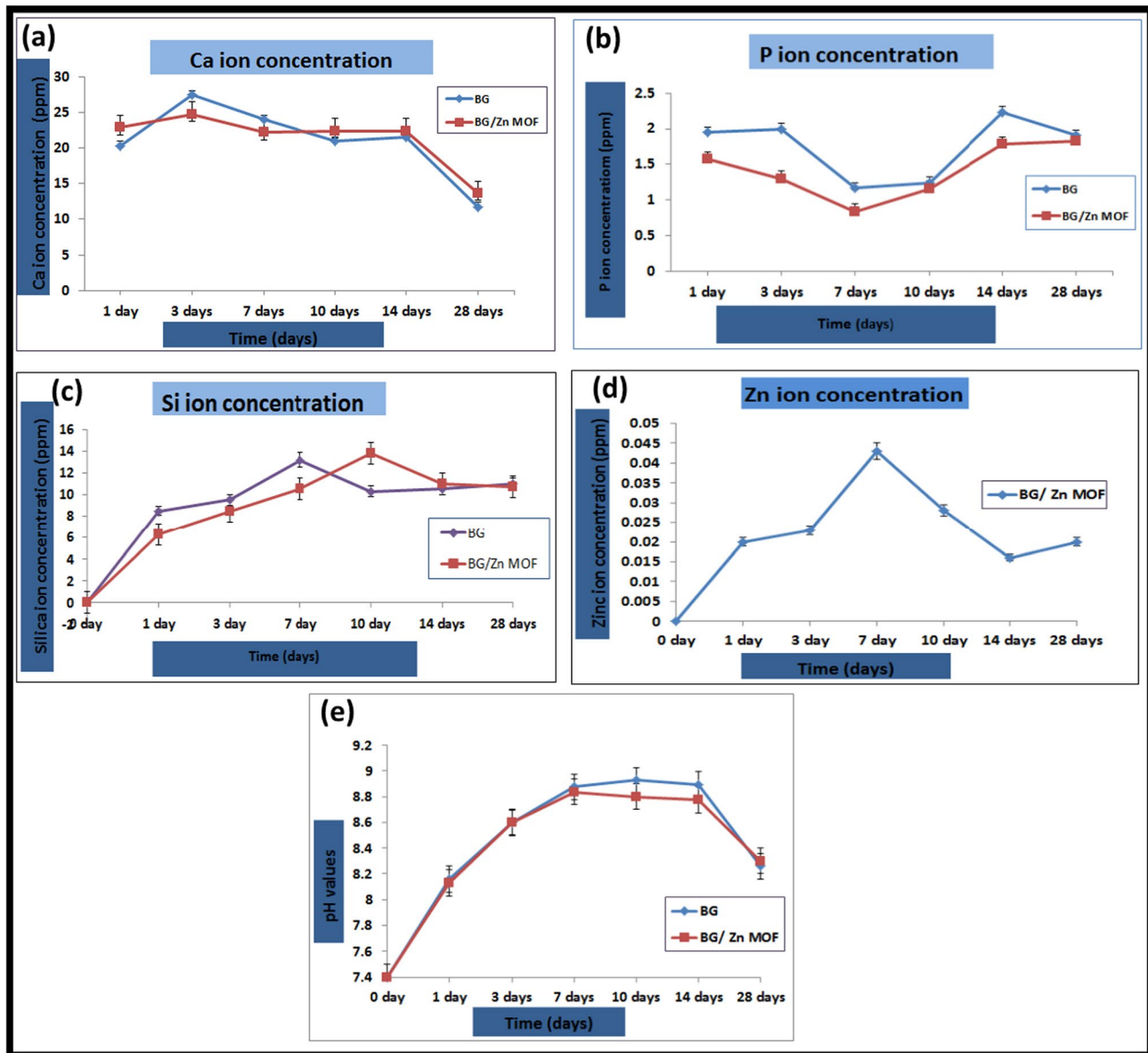


**Fig. 8** Ion concentration and pH changes at different periods for prepared samples

of decreased toxicity, it is also attributed to the increased ability of hydroxyapatite formation in addition to its advantageous antibacterial effect [39].

The pH of the SBF-incubated samples varied similarly (Fig. 8e), where the pH was raised in the first day of incubation from 7.40 to about  $8.15 \pm 0.05$  for BG sample and  $8.13 \pm 0.02$  for BG/Zn MOF. The increase in pH values continues until the tenth day ( $8.92 \pm 0.09$ , and  $8.80 \pm 0.02$  for BG, and BG/Zn MOF, respectively), then begins to decrease gradually until it reaches  $8.26 \pm 0.05$  and  $8.30 \pm 0.03$  for BG and BG/Zn MOF, respectively, at the end of soaking time. These findings could be explained as follows: at the early stages of incubation, the dissolution of samples takes place

leading to  $\text{Ca}^{2+}$ , and Si leaching out from samples, so pH increase occurs rapidly [39]; the  $\text{Zn}^{+2}$  release does not contribute to change in pH due to its low content in BG/Zn MOF sample. The decrease in pH may be ascribed to  $\text{Ca}^{+2}$  ions precipitation on the surface of the samples due to the attraction of the negative charge of Si–OH groups [46].

### 8.8 In vitro drug releasing kinetics in phosphate buffer solution (PBS)

Figure 9a represents the concentration of gentamicin loaded on BG and BG/Zn MOF. The results illustrate that

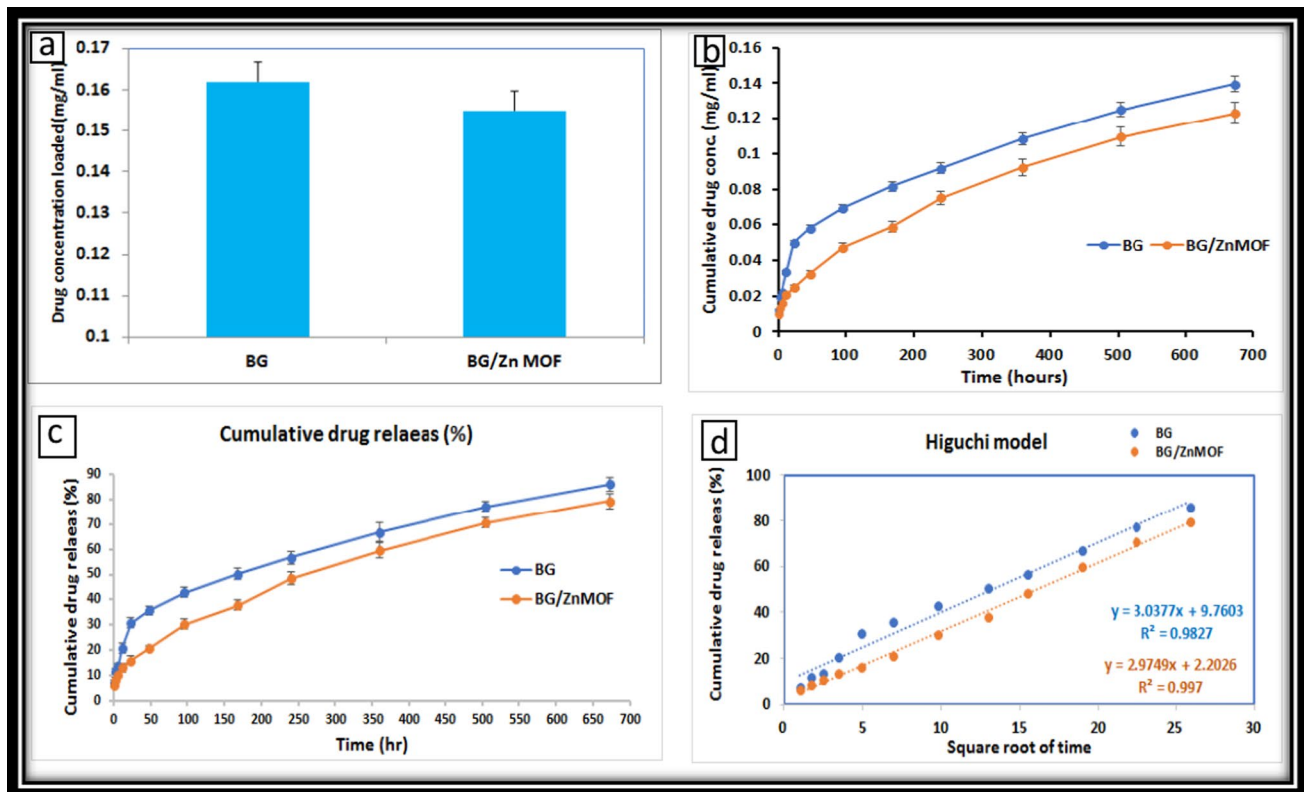


**Fig. 9** a Mass of loaded drug, b drug cumulative concentration release (mg/ml), c drug cumulative concentration release percentage, d fitting of drug data with Higuchi model

gentamicin was successfully loaded onto both samples. From the figure, it was noticed that BG/Zn MOF nanoparticles adsorbed a slightly lower quantity of drug ( $0.1550 \pm 0.005$  mg) than BG sample ( $0.1620 \pm 0.0049$  mg). However, the amount of loaded drug was non-significantly different.

Figure 9b represents the in vitro cumulative release profile of gentamicin of BG and BG/Zn MOF samples for 28 days. The drug release rate was affected by introducing Zn MOF nanoparticles to the BG sample, as indicated in Fig. 9b, c.

As shown in the figures, drug release occurs in two stages for all samples, beginning with a fast release caused by the rapid release of drug molecules at the material surface as a result of the water attack and continuing with a slow release caused by persistent drug release via pores. Thus, long-term release behavior from samples was achieved. The fast release ended at 24 h and the second gradual release started for both samples.

The burst release during 24 h was about 30.74% and 15.95% of the total amount of absorbed drug for BG and BG/Zn MOF, respectively; this burst release delivers plenty amount of drug doses that could terminate harmful bacteria. By contrast, the subsequent gradual release prevents bacterial re-growth or spreading to other parts.

After 28 days, the final cumulative percentage of drug released was about 86.082% and 79.32% of the loaded drug for BG and, BG/Zn MOF, respectively, Fig. 9c.

It was observed that both samples were still loaded with more amount of drug for further release. Moreover, the BG/Zn MOF sample presented a relatively slower rate of liberation (it reached 79.32% at the end of soaking time). This behavior may be due to the sluggish collapse of the MOFs in based media as illustrated previously [47].

Therefore, both samples, especially BG/Zn MOF, could transport extra drug doses for long periods (> 28 days), which could be valuable for patients suffering from bacterial bone infection disorder [48].

The drug release mechanism is defined by fitting the data by Higuchi model [49, 50] (Fig. 9d). All samples displayed good linear fitting with the Higuchi model, as can be observed from high values of  $R^2$  that nearly equal unity (0.9827 and 0.9970) for the BG and BG/Zn MOF samples, respectively. The drug was released at a rate of 3.037 and 2.974  $d^{-0.5}$  for the previous samples. This finding exhibited that the drug release mechanism for both samples was examined through controlled diffusion.

## 8.9 Cytotoxicity test

In vitro cytocompatibility studies were investigated to predict the biological reactions of materials when applied in vivo [51]. In vitro cell viability (SRB assay) studies were performed on human osteoblast-like cell cultures (MG-63), which have the same physiology and adhesiveness as human osteoblast cells [52]. The cell viability percent against different concentrations (100 and 300 µg/ml) of BG and BG/Zn MOF samples are illustrated in Fig. 10.

At both concentrations 100 or 300 µg/ml, there was no cytotoxic effect for all samples. At 100 µg/ml, the percentage of viable cells was  $101.07 \pm 1.92$  and  $102.09 \pm 2.41$  for BG and BG/Zn MOF, respectively.

It is seen that the prepared materials enhance cell proliferation, because they contain elements that have osteogenic properties [13, 15, 53]. Even at higher concentrations (300 µg/ml), the prepared materials showed excellent biocompatibility, with the percentage of live cells reaching  $97.14 \pm 0.82$  and  $96.79 \pm 1.20$  for BG and BG/Zn MOF, respectively.

The cell morphology was clarified by optical microscope examination with sample concentrations; of 100 and 300 µg/ml (Fig. 11). The results showed that all samples had no toxicity after 72 h of incubation. Where the untreated MG-63 cells were formed of union monolayer of spindle-shaped cells. Concerning control, no morphological variations were noticed in the osteoblast-like cells treated with prepared materials and cells spread well with a spindle-shaped appearance, rather than a round shape. Figure 11 demonstrates the survival of MG-63 cells. Therefore, all prepared materials were biocompatible,

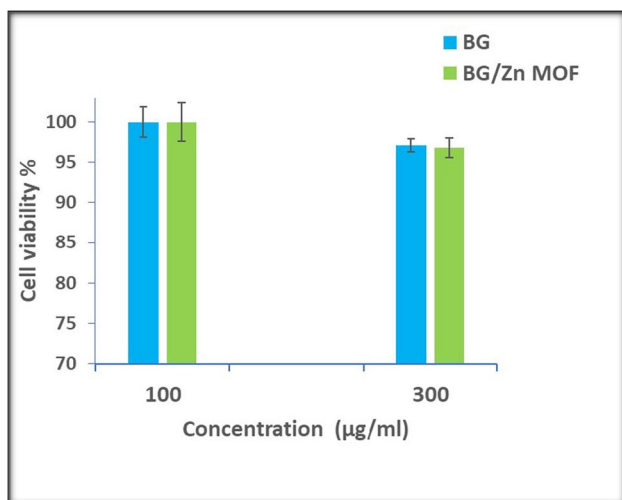


**Fig. 10** Cell viability percent against different concentrations of the prepared samples ( $p < 0.05$ )

had no toxic effect on cells, and could be safely used as biocompatible materials for bone regeneration.

## 8.10 In vitro antimicrobial behavior

The prepared samples (BG&BG/Zn MOF) were examined for antimicrobial activity with and without antibiotic. Table 3 and Fig. 12 illustrate the inhibition zone diameter (mm) of samples against various microorganisms. This test was performed on gram-positive and gram-negative bacteria (*Staphylococcus aureus* and *Escherichia coli*), as well as antifungal activity (*Candida albicans*).

All samples exhibited the presence of an inhibition zone against all examined microorganisms either with or without gentamicin. When the drug was not used, the sample containing zinc MOF (BG/Zn MOF) had significantly higher inhibitory activity than the sample containing glass-only (BG) for bacterial species ( $p < 0.05$ ). However, for fungi, BG showed an increase in inhibition zone than BG–Zn MOF.

The inhibition zone diameters created by BG were  $15.33 \pm 1.15$ ,  $11.00 \pm 0.00$ , and  $19.33 \pm 1.15$  for *Escherichia coli*, *Staphylococcus aureus*, and *Candida albicans*, respectively, while the zone caused by BG/Zn MOF was  $17.66 \pm 1.15$ ,  $13.33 \pm 3.21$ , and  $16.33 \pm 1.15$ , respectively (Table 3).

After mixing the prepared samples with the drug, the inhibition zone diameter was significantly increased ( $p = 0.03$ ) for all samples against different microorganisms. This means that the drug kept its antimicrobial activity after binding to the prepared samples. The inhibition zones range from  $25.66 \pm 0.66$  to  $37 \pm 1.15$  mm. It is worth noticing that the sample containing MOF mixed with the drug had the greatest inhibition zones for all tested microbes.

This antimicrobial activity of samples is due to the liberation of alkaline ions, such as calcium and zinc, that increase osmolarity, osmotic pressure, and pH of the culture media, hence affecting microbial growth [42]. Moreover, for BG/Zn MOF sample, the interaction of the prepared nanoparticles with the cell walls of fungi or bacteria causes leakage of  $Zn^{2+}$  ions. Consequently, this process leads to the formation of reactive oxygen species, which in turn disrupts the integrity of the microbial cell wall, ultimately resulting in its demise [54–57].

In gentamicin-loaded nanoparticles (Drug @BG, and Drug @BG/Zn MOF), the inhibitory activity of samples increased, and the drug maintained its antimicrobial efficacy. Gentamicin affects microbes by disrupting the integrity of the cell wall, leading to lysis of the cell. This disruption occurs sequentially, moving from the outer membrane to the inner membrane. Exposure to gentamicin results in a loss of protein and lipopolysaccharide from the outer membrane, as well as altered banding patterns of outer membrane proteins

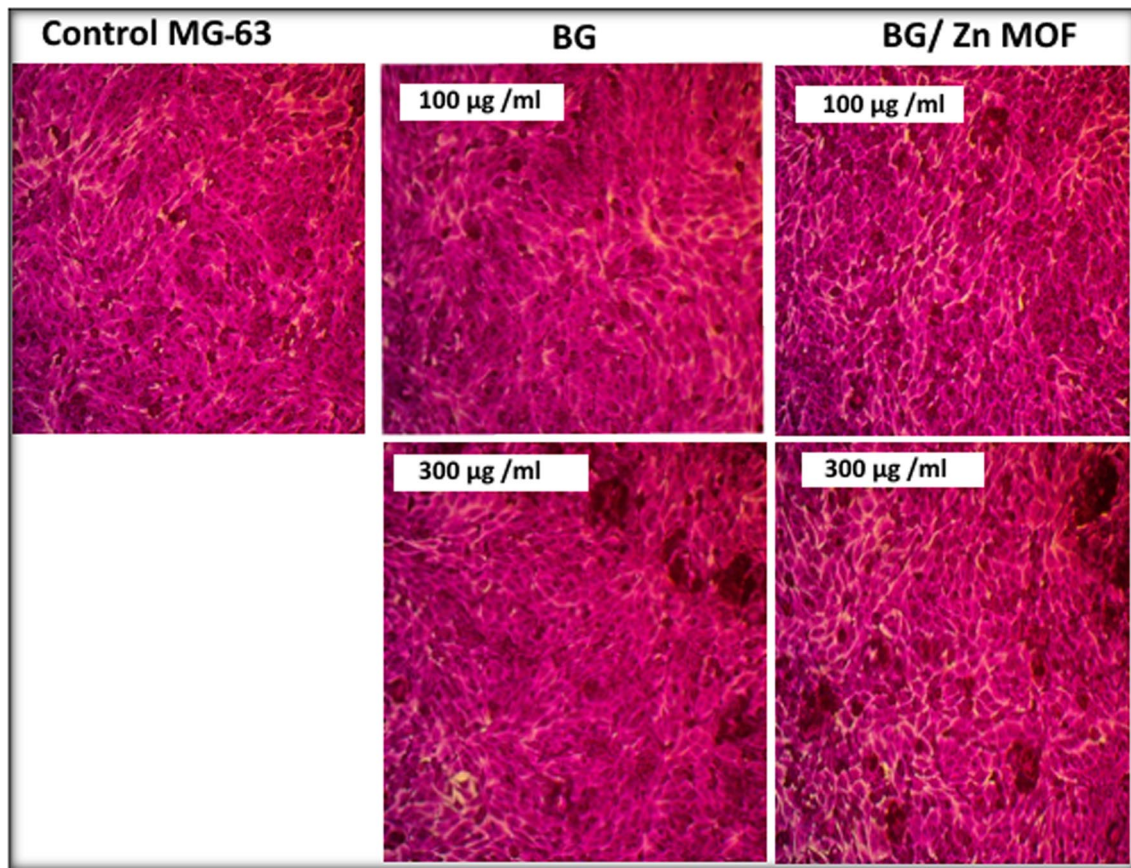


**Fig. 11** Optical microscopic photos (20× magnification) of MG-63 cells with the prepared samples at concentrations; 100 and 300 µg/ml

**Table 3** Inhibition zone diameter (millimeter) of the samples

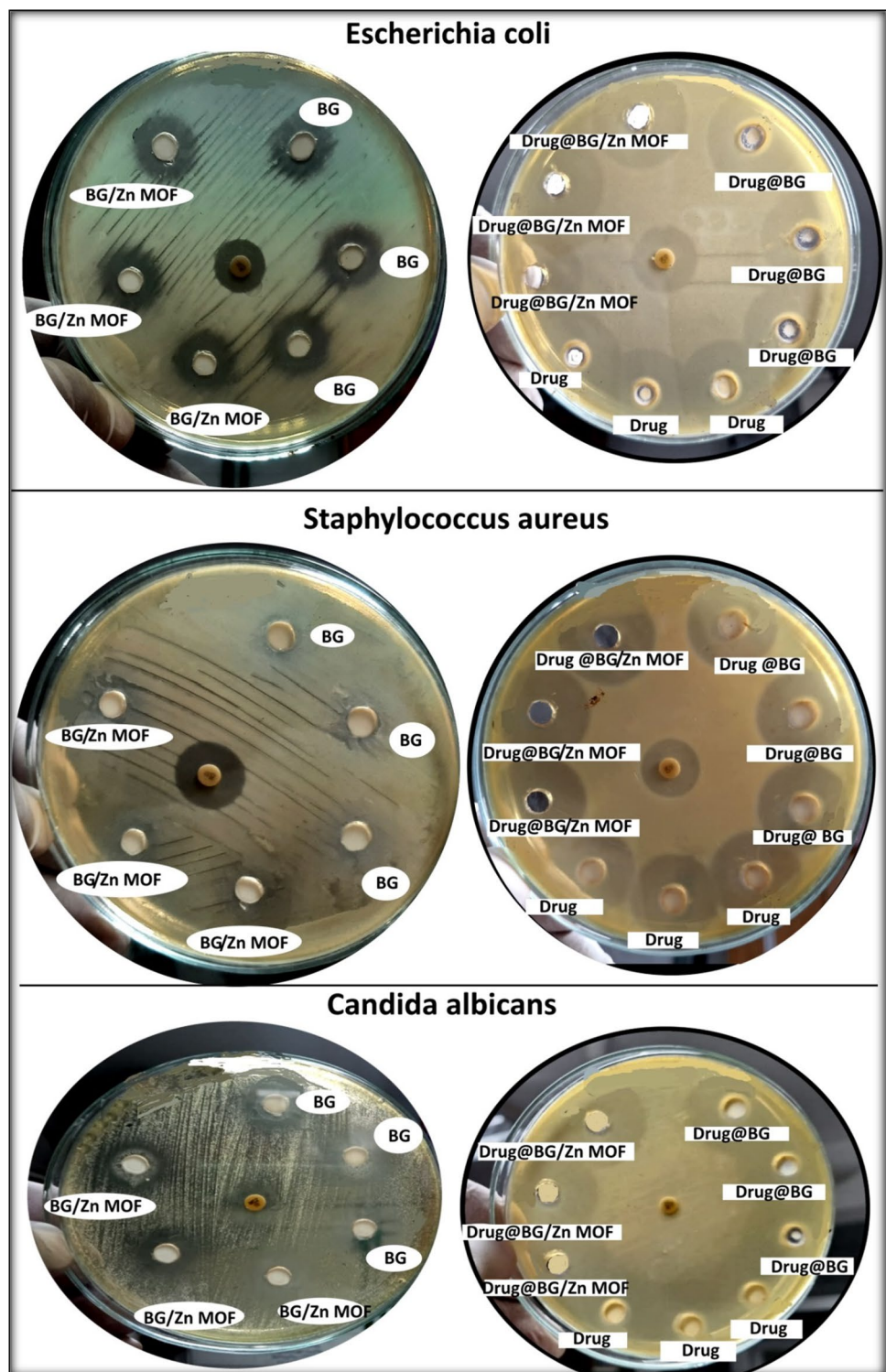
Test microorganisms	Samples						References	
	Diameter of inhibition zone (mm)						Gentamicin 10 mcg	Miconizol 10 mcg
	BG	BG/Zn MOF	Drug @BG	Drug @BG/Zn MOF	Drug			
<i>Escherichia coli</i> (ATCC 25922)	15.33 ± 1.15	17.66 ± 1.15	25.66 ± 0.58	30.33 ± 0.57	27.66 ± 0.57	16.00 ± 1.41	–	
<i>Staphylococcus aureus</i> (ATCC 6538)	11.00 ± 0.00	13.33 ± 3.21	26.66 ± 0.58	30.33 ± 1.15	28.00 ± 0.00	20.00 ± 1.41	–	
<i>Candida albicans</i> (ATCC 10231)	19.33 ± 1.15	16.33 ± 1.15	28.67 ± 1.54	37.33 ± 1.15	34.67 ± 1.15	–	10.0 ± 0.00	

[20, 58–60]. Gentamicin also decreases the magnesium and calcium content in the cell envelopes. It is thought that gentamicin displaces critical metal cations within the outer membrane, destabilizing and removing organic components [61]. Overall, the mechanism of action of gentamicin involves inhibiting protein synthesis and enhancing intracellular killing of microorganisms.

## 9 Conclusion

In the present work, Zn-MOF/bioactive glass nanoparticles were successfully prepared using quick-alkali-mediated sol–gel. Different characterizations of the prepared materials were assessed. The results illustrated that the addition of Zn MOF to bioactive glass increased the specific

**Fig. 12** Antimicrobial effects of the tested samples against different microorganisms



surface area and dispersity of nanoparticles. Moreover, it improved hydroxyapatite formation and caused Ca/P to approach stoichiometric apatite value ( $\text{Ca/P} = 1.67$ ). In addition, no morphological differences were observed in the osteoblast-like cells (MG-63) treated with prepared materials and prepared materials were biocompatible. In

addition, the nanoparticles were functionalized by gentamicin drug to solve the problem of probable infection related to orthopedic implantation surgeries. Gentamicin was successfully loaded into nanoparticles while retaining its antimicrobial properties. Therefore, it may be concluded that the prepared nanoparticles loaded with

gentamicin can be used as a potential approach for bone regeneration.

**Acknowledgements** The authors would like to thank the National Research Centre and Faculty of Science, Al-Azhar University (Girls), Egypt for the possibility to use their facilities.

**Author contributions** All authors have taken full responsibility for the content of this manuscript.

**Funding** Open access funding provided by The Science, Technology & Innovation Funding Authority (STDF) in cooperation with The Egyptian Knowledge Bank (EKB). The authors declare that no funds, grants, or other support were received during the preparation of this manuscript.

**Data availability** The data in the current study are available from the corresponding author on reasonable request.

## Declarations

**Conflicts of interest** The authors declare that they have no conflict of interest.

**Ethical approval** All cell culture experimental protocols were in accordance with the ethical guidelines of the ethical committee of National Research Centre.

**Open Access** This article is licensed under a Creative Commons Attribution 4.0 International License, which permits use, sharing, adaptation, distribution and reproduction in any medium or format, as long as you give appropriate credit to the original author(s) and the source, provide a link to the Creative Commons licence, and indicate if changes were made. The images or other third party material in this article are included in the article's Creative Commons licence, unless indicated otherwise in a credit line to the material. If material is not included in the article's Creative Commons licence and your intended use is not permitted by statutory regulation or exceeds the permitted use, you will need to obtain permission directly from the copyright holder. To view a copy of this licence, visit <http://creativecommons.org/licenses/by/4.0/>.

## References

1. I. Roohani, G.C. Yeo, S.M. Mithieux, A.S. Weiss, *Curr. Opin. Biotechnol.* **74**, 220 (2022)
2. J. Crush, A. Hussain, K.T.M. Seah, W.S. Khan, *Front. Cell Dev. Biol.* **9**, 1 (2021)
3. M. Lallukka, A. Houaoui, M. Miola, S. Miettinen, J. Massera, E. Verné, *Ceram. Int.* **49**, 36044–36055 (2023)
4. F. Unal, C. Tasar, B. Ercan, *Ceram. Int.* **49**, 20118 (2023)
5. M. Hosseini, N. Hassani Besheli, D. Deng, C. Lievens, Y. Zuo, S.C.G. Leeuwenburgh, F. Yang, *Biomater. Adv.* **144**, 213198 (2023)
6. J.R. Jones, *Acta Biomater.* **9**, 4457 (2013)
7. C. Wu, J. Chang, *J. Control. Release* **193**, 282 (2014)
8. M. Cannio, D. Bellucci, J.A. Roether, D.N. Boccaccini, V. Cannillo, *Materials (Basel)*. **14**, 1 (2021)
9. A. Shearer, M. Montazerian, J.J. Sly, R.G. Hill, J.C. Mauro, *Acta Biomater.* **160**, 14 (2023)
10. S. Tajvar, A. Hadjizadeh, S.S. Samandari, *Int. Biodeterior. Biodegrad.* **180**, 105599 (2023)
11. O.D. Abodunrin, K. El Mabrouk, M. Bricha, *J. Mater. Chem. B* **11**, 955 (2023)
12. F.V. Harzand, S. Navid, M. Nejad, A. Babapoor, S.M. Mousavi, *Symmetry (Basel)*. **15**, 403 (2023)
13. G. Luo, Y. Jiang, C. Xie, X. Lu, *Biosurface and Biotribology* **7**, 99 (2021)
14. Z. Zhang, S. Yin, X. Li, Y. Wang, K. Zhang, J. Li, *Metals (Basel)*. **13**, 1511 (2023)
15. Y. Pan, J. Wang, Z. Jiang, Q. Guo, Z. Zhang, and J. Li, *Sci. Reports* | **12**, 1 (2022).
16. R. Sacourbaravi, Z. Ansari, A. Mohammad, K. Valiollah, N. Esmaeil, *J. Inorg. Organomet. Polym. Mater.* **30**, 4615 (2020)
17. M. Moaness, M. Mabrouk, M.M. Ahmed, D.B. Das, H.H. Beherei, *Int. J. Pharm.* **616**, 121559 (2022)
18. K. Zheng, A.R. Boccaccini, *Adv. Colloid Interface Sci.* **249**, 363 (2017)
19. M.M. Ahmed, W.M. Abd-Allah, A.E. Omar, A.A.F. Soliman, *J. Inorg. Organomet. Polym. Mater.* **30**, 3646 (2020)
20. M.H. Hu, P.Y. Chu, S.M. Huang, B.S. Shih, C.L. Ko, J.J. Hu, W.C. Chen, *Biomimetics* **7**, 1 (2022)
21. J. McFarland, *J. Am. Med. Assoc.* **XLIX**, 1176 (1907)
22. A. El-Anssary, G. Abdel Raouf, H. El-Masry, *J. Herbmmed Pharmacol.* **10**, 476 (2021)
23. B.R. Barrioni, E. Norris, S. Li, P. Naruphontjirakul, J.R. Jones, M.M. de Pereira, *J. Mater. Sci. Mater. Med.* **30**, 382 (2019)
24. H.T. Sam, J.P. Gowsihan, P. Shu, B. Yu, J.V. Hanna, J.R. Jones, *Intrnational J. Appl. Glas. Sci.* **8**, 372 (2017)
25. S. Gwardiak, B. Szczeńśniak, J. Choma, M. Jaroniec, *J. Porous Mater.* **4**, 312 (2019)
26. S.A. Jasim, H.I.M. Amin, A. Rajabizadeh, M.A.L. Nobre, F. Borhani, A.T. Jalil, M.M. Saleh, M.M. Kadhim, M. Khatami, *Water Sci. Technol.* **86**, 2303 (2022)
27. Z. Neščáková, K. Zheng, L. Liverani, Q. Nawaz, D. Galusková, H. Kaňková, M. Michálek, D. Galusek, A.R. Boccaccini, *Bioact. Mater.* **4**, 312 (2019)
28. T. Aydemir, J.I. Pastore, E. Jimenez-Pique, J.J. Roa, A.R. Boccaccini, *J. Ballarre, Thin Solid Films* **732**, 138780 (2021)
29. R. Tejido-Rastrilla, S. Ferraris, W.H. Goldmann, A. Grünewald, R. Detsch, G. Baldi, S. Spriano, A.R. Boccaccini, *Materials (Basel)*. **12**, 500 (2019)
30. M. Mabrouk, H.H. Beherei, Y. Tanaka, M. Tanaka, *Int. J. Mol. Sci.* **22**, 8038 (2021)
31. S. Singh, A. Bharti, V.K. Meena, *J. Mater. Sci. Mater. Electron.* **25**, 3747 (2014)
32. D. Hendrix, J. McKeon, K. Wille, *Materials (Basel)*. **12**, 1976 (2019)
33. M.A. Azevedo, A.I. Bourbon, A.A. Vicente, M.A. Cerqueira, *Int. J. Biol. Macromol.* **71**, 141 (2014)
34. K. Thanawuth, S. Limmatvapirat, C. Rojviriya, P. Sriamornsak, *Pharmaceutics* **15**, 467 (2023)
35. S.A. Chew, M.A. Arriaga, V.A. Hinojosa, *J. Biomed. Mater. Res. - Part A* **104**, 1202 (2016)
36. Z.A. Alothman, *Materials (Basel)*. **5**, 2874 (2012)
37. A.E. Omar, M.M. Ahmed, W.M. Abd-Allah, *SILICON* **14**, 11171 (2022)
38. M.M. Ashour, M. Mabrouk, I.E. Soliman, H.H. Beherei, K.M. Tohamy, *IET Nanobiotechnol.* **15**, 291 (2021)
39. S. Chajri, S. Bouhazma, I. Adouar, S. Herradi, M. Khaldi, B. El Bali, M. Lachkar, *J. Phys. Conf. Ser.* **1292**, 012023 (2019)
40. M. Głab, S. Kudłacik-Kramarczyk, A. Drabczyk, J. Walter, A. Kordyka, M. Godzierz, R. Bogucki, B. Tyliczczak, A. Sobczak-Kupiec, *Molecules* **26**, 4268 (2021)
41. I. Mobasherpour, M.S. Heshajin, A. Kazemzadeh, M. Zakeri, *J. Alloys Compd.* **430**, 330 (2007)
42. A.E. Omar, H.S. Zayed, E.M.A. Hamzawy, *Appl. Phys. A* **128**, 76 (2021)



43. G. Stanciu, I. Sandulescu, B. Savu, S. Stanciu, K. Paraskevopoulos, X. Chatzistavrou, E. Kontonasaki, P. Koidis, J. Biomed. Pharm. Eng. **1**, 34 (2007)
44. X.V. Bui, T.H. Dang, *Process. Appl. Ceram.* **13**, 98 (2019)
45. S. Chajri, S. Bouhazma, S. Herradi, H. Barkai, S. EL ABED, I. Saad, B. El Bali, and M. Lachkar, **7**, 1882 (2016).
46. S.R. Gavinho, A.S. Pádua, I. Sá-Nogueira, J.C. Silva, J.P. Borges, L.C. Costa, M.P.F. Graça, *Materials (Basel)*. **16**, 956 (2023)
47. M. Al Haydar, H.R. Abid, B. Sunderland, S. Wang, *Drug Des. Devel. Ther.* **11**, 2685 (2017)
48. M.I. Hofstee, G. Muthukrishnan, G.J. Atkins, M. Riool, K. Thompson, M. Morgenstern, M.J. Stoddart, R.G. Richards, S.A.J. Zaat, T.F. Moriarty, *Am. J. Pathol.* **190**, 1151 (2020)
49. G. Singhvi, M. Singh, *Int. J. Pharm. Stud. Res.* **2**, 77 (2011)
50. S. Dash, P.N. Murthy, L. Nath, P. Chowdhury, *Acta Pol. Pharm. - Drug Res.* **67**, 217 (2010)
51. S. Chitra, P. Bargavi, S. Balakumar, J. Biomed. Mater. Res. - Part B Appl. Biomater. **108**, 143 (2020)
52. V.R. Sivaperumal, R. Mani, V. Poliseti, K. Aruchamy, T. Oh, *Molecules* **28**, 345 (2023)
53. P. Pei, Z. Tian, Y. Zhu, *Microporous Mesoporous Mater.* **272**, 24 (2018)
54. P. Mazur, I. Skiba-Kurek, P. Mrowiec, E. Karczewska, R. Drożdż, *Int. J. Nanomedicine* **15**, 3551 (2020)
55. D. Zhong, Y. Zuo, Y. Shi, P. Zhang, Y. Xu, B. Li, *Chem. Eng. J.* **460**, 141837 (2023)
56. M. Lv, M. Sun, M. Wu, F. Zhang, H. Yin, Y. Sun, R. Liu, Z. Fan, J. Du, *Nano Lett.* **22**, 9621 (2022)
57. Y. Chen, J. Cai, D. Liu, S. Liu, D. Lei, L. Zheng, Q. Wei, M. Gao, *Regen. Biomater.* **9**, rbac019 (2022)
58. F. Baquero, B.R. Levin, *Nat. Rev. Microbiol.* **19**, 123 (2021)
59. L. Shan, Q. Wenling, P. Mauro, B. Stefano, *Curr. Med. Chem.* **27**, 2902 (2020)
60. K.S. Rosenthal, K.M. Risley, *Infect. Dis. Clin. Pract.* **21**, 38 (2013)
61. N.L. Martin, T.J. Beveridge, *Antimicrob. Agents Chemother.* **29**, 1079 (1986)

**Publisher's Note** Springer Nature remains neutral with regard to jurisdictional claims in published maps and institutional affiliations.